# Dual Phase-Shift Symmetrical SVM Strategy Optimized by Dual Modulation Indices for Single-Stage Isolated DC–AC Matrix Converter

Guangcheng Ye, Hao Qin, Abhishek Kumar, *Senior Member, IEEE*, Ramesh C. Bansal, *Senior Member, IEEE*, Elena Gryazina, *Member, IEEE*, and Yan Deng, *Senior Member, IEEE*

***Abstract*—The single-stage, isolated three-phase dc–ac converter presents significant advantages for applications involving low dc voltages. By eliminating the need for large capacitors, this design facilitates a more compact physical layout. However, the complexity inherent in modulation strategies frequently gives rise to substantial three-phase current harmonics, which adversely affect system performance. Despite numerous efforts documented in the literature to enhance various performance metrics, the effectiveness of these solutions has often been found to be limited. This article presents a new modulation strategy designed to enhance the overall performance of high-frequency link matrix converters. We utilize frequency domain analysis through Fourier transform for our modeling approach. Our strategy optimizes performance by employing a combination of dual shift phase angles and dual modulation indices. Finally, the validation of this strategy was conducted on a three-phase 800 W prototype. Experimental outcomes demonstrated a Total Harmonic Distortion below 2% using a single DSP controller, corroborating theoretical model which predicted a reduction in current stress to 84% of its initial level, and the peak value of low-frequency fluctuation is reduced to 72–78%.**

***Index Terms*—Current distortion, frequency domain analysis (FDA), isolated dc–ac matrix converter (MC), phase-shift, space vector modulation (SVM).**

## I. Introduction

In present-day power networks, dc-based sources and loads have gained increasing prominence, appearing in areas such as electric vehicles (EV), data centers, communication infrastructure, and renewable energy systems like photovoltaic (PV) arrays and electrochemical storage units. Under these conditions, dc–ac converters serve as essential links to the power grid, ensuring that energy is transferred efficiently, stably, and safely. Traditionally, isolated ac–dc systems have adopted a two-stage architecture, as illustrated in Fig. 1(a). In this setup, the initial stage features a dc–dc converter that utilizes a high-frequency transformer (HFT) for electrical isolation, with a significant dc electrolytic capacitor acting as the intermediary to the back-end voltage source converters (VSCs).

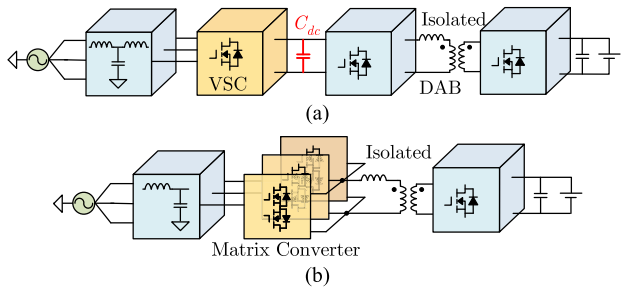


Fig. 1. AC-DC system structure. (a) Two-stages. (b) Single-stage.

However, the employment of these capacitors not only shortens system life, but also restricts the enhancement of power density. In response to these challenges, researchers have proposed the single-stage isolated ac–dc matrix converter (MC) as a promising solution [1]. As illustrated in Fig. 1(b), this configuration directly links the dc source or load to a HFT through an H-bridge. On the other side of the transformer, a single-phase to three-phase matrix converter (3-1MC) performs the voltage transformation. This setup, dubbed the high-frequency link matrix converter (HFLMC), parallels the structure of a single-phase dual active bridge (DAB) system [2], [3]. By eliminating the requirement for large capacitors, the HFLMC not only enhances power density but also prolongs system durability. Furthermore, its architecture inherently supports soft switching techniques, leveraging DAB control principles to elevate conversion efficiency [4], [5], [6]. When considering rectification, traditional VSCs operate in a boost mode, but the 3-1MC functions as a buck converter, making the HFLMC especially well-suited for low-voltage dc applications, like residential power systems.

The single-stage isolation, coupled with its adaptability to low dc voltages and the straightforward implementation of

Received 14 January 2025; revised 6 April 2025 and 28 June 2025; accepted 31 August 2025. Date of publication 9 September 2025; date of current version 22 October 2025. This work was supported by the National Key R&D Program of China under Grant 2025YFE0101600. Recommended for publication by Associate Editor J. I. Itoh. *(Corresponding author: Yan Deng.)*

Guangcheng Ye, Hao Qin, Abhishek Kumar, and Yan Deng are with the Research Group for Energy Network Transition (ReGENT), College of Electrical Engineering, Zhejiang University Hangzhou, Hangzhou 310027, China (e-mail: 22210075@zju.edu.cn; qinhaozju@zju.edu.cn; abhi@zju.edu.cn; dengyan@zju.edu.cn).

Ramesh C. Bansal is with the Department of Electrical Engineering, University of Sharjah, Sharjah, UAE, and also with the Department of Electrical, Electronic and Computer Engineering, University of Pretoria, Pretoria 0002, South Africa (e-mail: rcbansal@ieee.org).

Elena Gryazina is with the Center for Energy Science and Technology, Skolkovo Institute of Science and Technology (Skoltech), 121205 Moscow, Russia (e-mail: e.gryazina@skoltech.ru).

Color versions of one or more figures in this article are available at https://doi.org/10.1109/TPEL.2025.3608234.

Digital Object Identifier 10.1109/TPEL.2025.3608234

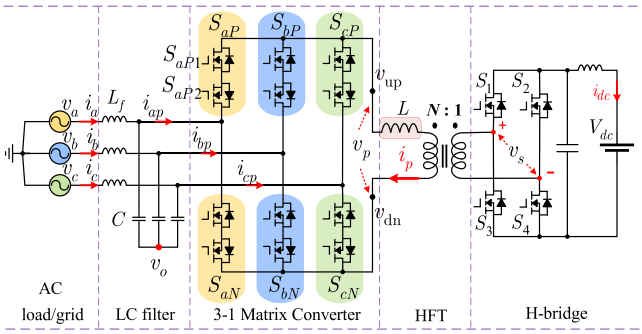


Fig. 2. Single-stage isolated bidirectional DC–AC topology (HFLMC).

zero-voltage switching (ZVS), makes the HFLMC a focal point of contemporary research, providing substantial practical advantages. Given the HFLMC's design benefits in eliminating large capacitors and enhancing power density, the core challenge shifts to its control mechanism. The intricate task involves harmonizing the H-bridge and the 3-1MC operations to secure bidirectional power flow while preserving current quality. This topology's popularity is not merely coincidental but a direct result of both the pressing needs of contemporary applications and the substantial strides in numerical control technology, which now enables the execution of more sophisticated control strategies [7].

Fig. 2 illustrates how the 3-1MC, which uses six bidirectional switches, effectively operates as two current source converters (CSCs) in antiphase and connected in parallel [8]. This setup ensures they work on the positive and negative half-cycles of the HFT to maintain ampere-second balance. Consequently, this has sparked extensive research into developing numerous PWM modulation strategies aimed at optimizing the performance of the HFLMC.

Following the operational dynamics of the HFLMC as outlined above, significant research has focused on refining PWM modulation strategies to enhance overall performance.

For soft switching, Das et al. [6] developed a novel modulation technique, applicable only when the peak line-to-line voltage remains below the dc voltage, thereby not fully exploiting the 3-1MC's buck-down capabilities. This strategy, while effective for soft switching, increases the number of switching actions.

Saha et al. [9] optimized the modulation strategy and established an accurate loss model, while Gorla et al. [10] further developed this approach. These works effectively reduced circuit loss while reducing the circuit cost, and achieved high power density and high efficiency.

Varajão et al. proposed an integration of Space Vector Modulation (SVM) with DAB-based phase-shifted modulation (PSM) to enable bidirectional power transfer [11]. However, this approach struggles with volt–second imbalance, leading to increased dc current ripple, higher Total Harmonic Distortion (THD), and an abundance of narrow pulses.

Sayed et al. [12] took a different approach with a carrier-based PWM strategy, where the duty cycle is calculated through a rectangular approximation. While this method does reduce switching actions, it compromises by introducing considerable harmonic distortion in the three-phase currents.

To address pulse width and THD issues, modifications to the six-segment SVM (6S-SVM) involved reallocating the duty cycle of zero vectors [13]. This technique, although reducing switching actions and offering frequency domain analysis (FDA) benefits, does not mitigate the dc-bias related current issues.

Hu et al. [14] introduced an asymmetrical SVM strategy adept at managing open-circuit faults. They further developed a dual-period decoupled modulation technique (DPD-SVPSM) to isolate transformer and grid currents, thus reducing THD [15], [16]. This method, however, relies heavily on precise timing control, with a subsequent variable dual-period modulation (VDPD-SVPSM) designed to push power limits [17].

Further efforts to minimize inductor current stress leveraged the 6S-SVM strategy, with the dynamic phase-shift angle of the H-bridge derived through both FDA and time-domain analysis (TDA) [18], [19]. Despite these advancements, the persistent challenge of dc-bias remained unaddressed.

Certain studies have focused solely on the uncontrolled rectification (ac–dc) direction. For instance, work presented in [20], based on 6S-SVM, solved the nonideal current equation via TDA and eliminated THD by adjusting the modulation index in real time. In addition, for specific conditions, abandoning zero vectors and altering vector sequences can reduce dc current ripple [21]. A comparative analysis of various 6S-SVM strategies was conducted in [4], aiding in the selection of methods that more readily achieve ZVS.

After recognizing the issue of dc-bias caused by line-to-line voltage, Hu [22] adopted a four-segment symmetrical space vector modulation (SSVM) (4S-SSVM) method. This approach suppresses narrow pulses, lowers switching frequency, and reduces the amplitude of common-mode voltage (CMV). Lan [23], [24] further analyzed why soft switching is more easily realized with this method.

Last, for dc to ac conversion, Jin [25] and Hu [26] employed an 8-segment 8S-SSVM, which, while reducing current stress, depends on specific timing arrangements leading to narrow pulses. A novel approach with an additional duty cycle closed-loop through current sampling was suggested to mitigate bias current and reduce CMV [27].

Overall, the performance of HFLMCs depends on managing current stress and ripple, ensuring proper HFT magnetic balance, controlling CMV amplitude, and avoiding narrow pulses, all while keeping implementation complexity and costs in check. Although previous research has yielded continuous improvements [6], [11], [12], [13], [14], gaps remain in covering all essential performance aspects. In addition, many TDA methods hinge on highly specific timing arrangements [18], [20], [25] or apply solely to uncontrolled rectification modes [4], [20], [21], [22], [23], [24], limiting their general applicability and leaving certain facets of HFLMC performance underexplored.

Recent enhanced strategies have attempted to address these shortcomings. For instance, while 6S-SVM introduces dc-bias and thus severe current peaks and ripple, SSVM mitigates these issues and reduces switching frequency and CMV. However, questions regarding cost, stability, and open-loop

feasibility remain. Moreover, uncontrolled rectification topologies operating in discontinuous conduction mode (DCM) fall short of dc–ac inverter requirements [22], [23], [24], [27]. Although symmetrical 8S-SVM enables inverter functionality, the TDA model employed is narrow in scope and lacks universal applicability [25]. Very recently, Sun et al. [28] proposed a zero-vector-reconfiguration based SVPWM for a high-frequency link three-phase ac–dc converter, achieving ZVZCS soft-switching and voltage spike suppression. Simultaneously, Rosas et al. [29] introduced a novel modulation and control strategy for a quad-active-bridge resonant-type single-stage three-phase ac-dc converter, utilizing only unipolar switches and demonstrating efficient bidirectional active-reactive power transfer capability for V2G applications. Nevertheless, these approaches still face challenges in terms of application scope limitations, potential implementation complexity, or the need for further validation under broader operating conditions, leaving room for more comprehensive solutions.

This article advances existing HFLMC modulation methods to offer a more comprehensive and versatile solution. The key contributions are as follows:

1) Introduces a Dual-Phase-Shift Coordinated Symmetrical SVM (DPS-SSVM) strategy with enhanced comprehensive performance, along with a novel method for correcting three-phase distorted currents, and this method can operate over a power factor (PF) range from 0 to 1.
2) Establishes a frequency-domain model supporting bidirectional power transfer, extending SSVM theory to arbitrary phase-shift angles and operating modes. This overcomes the limitations of TDA-based approaches and provides a universal modeling framework.
3) Achieves comprehensive performance enhancement, including lower current THD, reduced switching frequency, improved dc-bias suppression, halved CMV amplitude, elimination of narrow pulses, and minimal controller CPU utilization.

The rest of this article is organized as follows: Section II introduces the dual phase-shift SSVM (DPS-SSVM) strategy optimized by dual modulation indices for the HFLMC, detailing its basics, symmetrical modulation, Fourier modeling, current optimization, and simulation. Section III compares this strategy's performance against existing methods, focusing on current suppression, THD, dc-bias, and common mode voltage (CMV) reduction. Section IV provides experimental verification, including THD statistics, inductor current comparison, and additional benefits like switching actions and controller efficiency. Finally, Section V concludes this article.

## II. Proposed Dual Modulation Indices Strategy for HFLMC Topology

### A. Basic Rules of HFLMC

Building upon the foundational overview, this section delves into the proposed dual modulation indices strategy for the HFLMC topology. The HFLMC's primary components include a HFT and a 3-1MC. Each bridge arm of the 3-1MC comprises two bidirectional switches, denoted as $S_{xP}$ and $S_{xN}$, where $x$ represents the phases ($a$, $b$, $c$). These bidirectional switches consist of two IGBTs or MOSFETs connected in reverse series, facilitating a high-frequency conversion pathway for alternating current (ac).

TABLE I
Definition of Space Current Vector

| Space vectors | Switching status | | | | | | Output voltage |
|---|---|---|---|---|---|---|---|
| | $S_{aP}$ | $S_{aN}$ | $S_{bP}$ | $S_{bN}$ | $S_{cP}$ | $S_{cN}$ | $v_p$ |
| $I_1$(-$I_4$) | 1 | 0 | 0 | 1 | 0 | 0 | $v_{ab}$ |
| $I_2$(-$I_5$) | 1 | 0 | 0 | 0 | 0 | 1 | $v_{ac}$ |
| $I_3$(-$I_6$) | 0 | 0 | 1 | 0 | 0 | 1 | $v_{bc}$ |
| $I_4$(-$I_1$) | 0 | 1 | 1 | 0 | 0 | 0 | $v_{ba}$ |
| $I_5$(-$I_2$) | 0 | 1 | 0 | 0 | 1 | 0 | $v_{ca}$ |
| $I_6$(-$I_3$) | 0 | 0 | 0 | 1 | 1 | 0 | $v_{cb}$ |
| $I_7$ | 1 | 1 | 0 | 0 | 0 | 0 | $v_{aa}(0)$ |
| $I_8$ | 0 | 0 | 1 | 1 | 0 | 0 | $v_{bb}(0)$ |
| $I_9$ | 0 | 0 | 0 | 0 | 1 | 1 | $v_{cc}(0)$ |

The HFT is modeled with an energy storage inductor $L$ and an ideal voltage ratio $N$, interfacing the dc power supply or load through an H-bridge circuit, as depicted in Fig. 2.

Table I outlines the definitions of the nine current vectors associated with the 3-1MC. Given that the inductor current is a high-frequency ac, the modulation process of the 3-1MC can be effectively represented as two reverse-parallel CSCs. This equivalence underscores the necessity of preventing open circuits on the transformer side and ensures that the ac capacitor ($C_f$) voltage remains unswitched. The switching functions of each bidirectional switch are defined in (1), while the operational constraints are detailed as follows:

$$S_{xY} = \begin{cases} 1, & \text{turn on} \\ 0, & \text{turn off} \end{cases} \quad x = \{a, b, c\}, Y = \{P, N\} \tag{1}$$

$$\begin{cases} S_{aP} + S_{bP} + S_{cP} = 1 \\ S_{aN} + S_{bN} + S_{cN} = 1 \end{cases}. \tag{2}$$

The ideal output voltage of a three-phase symmetrical load is as follows:

$$v_g(t) = \begin{bmatrix} v_{ga}(t) \\ v_{gb}(t) \\ v_{gc}(t) \end{bmatrix} = V_m \begin{bmatrix} \cos(\omega t - \varphi) \\ \cos(\omega t - 2\pi/3 - \varphi) \\ \cos(\omega t + 2\pi/3 - \varphi) \end{bmatrix} \tag{3}$$

where $\omega$ represents the three-phase angular frequency, phase angle $\theta = \omega t$ is the angular displacement between the reference current and $\alpha$-axis. While $\theta \in (-30^\circ, 0)$, line to line voltage can be expressed as

$$\begin{bmatrix} v_{ab} \\ v_{ac} \end{bmatrix} = \sqrt{3} V_m \begin{bmatrix} \cos(\theta - \varphi + \pi/6) \\ \cos(\theta - \varphi - \pi/6) \end{bmatrix}. \tag{4}$$

Based on the principle of SVM, a power frequency cycle can be divided into 12 sectors. Fig. 3 illustrates that in SVM modulation, each rotating reference current vector is composed of two adjacent basic current vectors. The current path is selected through a bidirectional switch, and the three-phase line voltage is applied to the primary voltage ($v_p$). Positive and negative current vectors each occupy half of the modulation period to meet the requirements of ampere–second balance. The subsequent theoretical analysis in this article takes the 12th sector as an

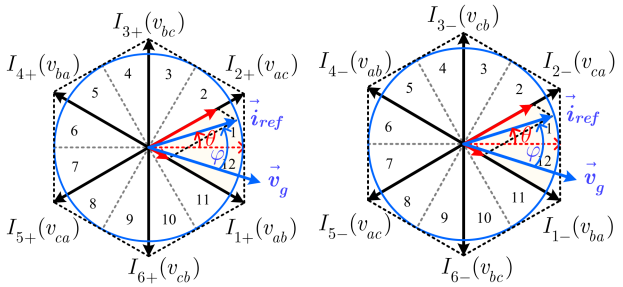


Fig. 3. Space vector synthesis relationship.

example (phase angle $\theta \in (-30°, 0)$), and the ampere–second balance rule is as follows:

$$I_{\text{ref}} T_s = I_1 T_1 + I_2 T_2 + I_0 T_0$$
$$T_0 = T_s - T_1 - T_2. \tag{5}$$

According to the vector synthesis rule, the duration of the current vectors is calculated as

$$T_1 = m_1 T_s \sin(\pi/6 - \theta)$$
$$T_2 = m_2 T_s \sin(\pi/6 + \theta)$$
$$T_0 = T_s - T_1 - T_2 \tag{6}$$

where $m_1$ and $m_2$ are the modulation indices of the main vector $I_1$ and the sub vector $I_2$, respectively. In conventional strategies, the modulation index use the same parameters $m$.

The secondary voltage ($v_s$) is obtained by converting the dc voltage through the H-bridge. The voltage difference between the primary and secondary sides will be alternately applied to the energy storage inductor $L$ as the high-frequency switches are turned ON and OFF. The 3-1MC controls different current vectors, and the relationship between each branch current ($i_{xp}$) and the high-frequency inductor current ($i_p$) is

$$(S_{xP} - S_{xN}) \cdot i_{xp} = i_p, x = \{a, b, c\}. \tag{7}$$

The high-frequency current on the inductor is filtered by the capacitor and outputs a three-phase current waveform.

### B. Proposed Modulation Strategy

The modulation waveform combining SVM and PSM is shown in Fig. 4, which represents the proposed DPS-SSVM strategy in this article.

The secondary voltage is composed of four switches on the H-bridge that undergo two phase-shifts. The variable $\phi_1$ determines the phase-shift angle (primary phase-shift angle) of $v_s$ relative to the beginning of the cycle (time $t = t_0$), and $\phi_2$ determines the internal phase-shift angle (secondary phase-shift angle) of $v_s$, which affects the duty cycle of the positive/negative voltage in one switching cycle.

DPS-SSVM is fundamentally derived from the symmetrical 4-Segment SVM (4S-SVM) used in ac–dc uncontrolled rectification modes [22], [23]. Although the primary voltage waveform maintains a similar form, this article introduces a dual phase-shift mode on the H-bridge to accommodate the dc–ac inverter functionality.

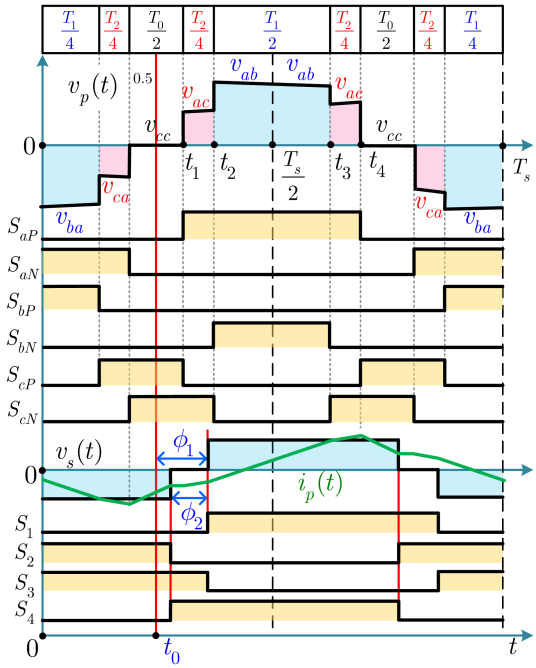


Fig. 4. Key waveforms and signals of DPS-SSVM modulation strategy.

Through frequency-domain modeling, the THD issues associated with SSVM in the dc–ac direction are identified. To mitigate these inherent drawbacks, dual modulation indices ($m_1$ and $m_2$) are optimized, significantly enhancing the overall performance of the strategy.

Also, it is critical to maintain appropriate duty cycles for the switch drive signals. Duty cycles that are too small or too large can prevent the switch devices from responding correctly to modulation commands, resulting in what are known as narrow pulses. Narrow pulses can severely disrupt the normal operation of the circuit. Specifically, when the duty cycle of a switch signal is less than 3% of the switch period ($T_s$), it is classified as a narrow pulse [13]. Fig. 5 illustrates the calculation results of narrow pulse content across different modulation strategies, with the modulation index ($m$) and phase angle ($\theta$) serving as independent variables.

### C. Fourier Modeling of HFT

Variations in the two phase-shift angles can complicate the classification and analysis when utilizing time-domain methods for SVM modeling. As a result, many studies on SVM modeling are constrained by specific temporal conditions. To address these challenges, this article employs Fourier series to represent the primary voltage and secondary voltage. This approach allows us to bypass the complexities of TDA by relying solely on trigonometric series expressions. Beginning at $t = t_0$ as the cycle reference point, the relevant definitions are as follows:

$$v_p(t) = \sum_{n=1,2,3}^{\infty} [a_p(n)\cos(n\omega_s t) + b_p(n)\sin(n\omega_s t)]$$

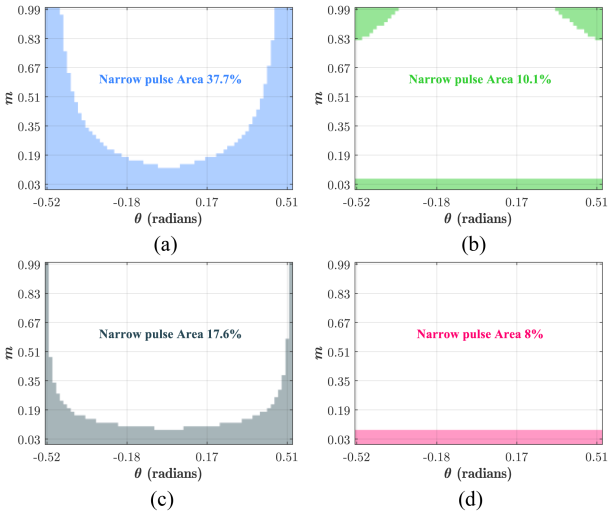


Fig. 5. Narrow pulses occurrence area (colored part) related to modulation index in sectors 12 and 1, with a narrow pulse threshold of 3% *Ts*. (a) Area 37.7% in [18], [20], [23], [25], [26]. (b) Area 10.1% in [13]. (c) Area 17.6% in [11]. (d) Area 8% in this paper.

$$v_s(t) = \sum_{n=1,2,3}^{\infty} a_s(n)\cos(n\omega_s t - n\phi_1) + \sum_{n=1,2,3}^{\infty} b_s(n)\sin(n\omega_s t - n\phi_1) \tag{8}$$

where $\omega_s$ is the switching angular frequency, and the Fourier coefficients are calculated by the following:

$$a_x(n) = \frac{2}{T}\int_{t_0}^{t_0+T} v_x(t)\cos(n\omega_s t)dt$$
$$b_x(n) = \frac{2}{T}\int_{t_0}^{t_0+T} v_x(t)\sin(n\omega_s t)dt \tag{9}$$

where $x = \{p, s\}$, and the results of each coefficient are

$$\begin{bmatrix} a_s(n) \\ b_s(n) \end{bmatrix} = \frac{2V_{dc}}{n\pi}\begin{bmatrix} \sin(n(\pi-\phi_2)) \\ 1-\cos(n(\pi-\phi_2)) \end{bmatrix}, n = 1,3,5, \tag{10}$$

$$a_p(n) = 0$$
$$b_p(n) = \frac{4\sqrt{3}}{n\pi}V_m \sin\left(\frac{n\pi}{2}\right) \times \begin{pmatrix} \sin(\theta-\varphi)\cdot\sin(\frac{n\pi}{2}m\sin(\theta-\frac{\pi}{6})) \\ +\cos(\theta-\frac{\pi}{6}-\varphi)\cdot\sin(\frac{n\pi}{2}m\cos\theta) \end{pmatrix}. \tag{11}$$

The voltage current relationship and periodic relationship of the energy storage inductor ($L$) are

$$L\cdot di_p(t) = (v_p(t) - Nv_s(t))\cdot dt$$
$$i_p(0) = -i_p(T_s/2). \tag{12}$$

The result of integrating the above equation to obtain the inductor current ($i_p$) is

$$i_p(t) = \frac{1}{\omega_s L}\sum_{n=1}^{\infty}\frac{1}{n}(A_n\cos(n\omega_s t) + B_n\sin(n\omega_s t))$$

TABLE II
SIMULATION AND EXPERIMENTAL PARAMETERS

| Parameters | Values |
|---|---|
| DC voltage | 45V~90V |
| AC phase voltage peak value / load | 130V~160V (50Hz) / 48Ω |
| Power rating | 800W |
| Turns ratio of HFT | 1:1 |
| Power inductor (PQ50/50) | 70uH |
| CL filter (AC side) | 6.6uF, 2mH |
| Switching frequency | 20kHz |
| Switching device (IGBT) | FGW40G120WD |
| Controller (DSP) | TMS320F28377D |

$$\begin{bmatrix} A_n \\ B_n \end{bmatrix} = N\begin{bmatrix} a_s(n) & b_s(n) \\ b_s(n) & -a_s(n) \end{bmatrix}\cdot\begin{bmatrix} \sin(n\phi_1) \\ \cos(n\phi_1) \end{bmatrix} + \begin{bmatrix} -b_p(n) \\ a_p(n) \end{bmatrix} \tag{13}$$

where the $b_p(n)$ term including the power angle ($\varphi$) relationship is only related to $A_n$, and the even order terms of $a_x(n)$ and $b_x(n)$ are both 0. Subsequently, these analysis results can be rewritten in phasor form (14). Thus, the expression for the peak current of the inductor is obtained in (15), which facilitates performance comparison with other modulation methods.

$$U_P = \frac{v_p}{\sqrt{2}} = \sum_{n=1}^{\infty}\frac{b_p(n) + ja_p(n)}{\sqrt{2}}$$
$$U_S = \frac{v_s}{\sqrt{2}} = \sum_{n=1}^{\infty}\left[\frac{a_s(n)}{\sqrt{2}}e^{j\left(\frac{\pi}{2}-n\phi_1\right)} + \frac{b_s(n)}{\sqrt{2}}e^{-jn\phi_1}\right]$$
$$I_P = \sum_{n=1}^{\infty}\frac{U_P - NU_S}{jn\omega_s L} = \sum_{n=1}^{\infty}\frac{B_n + jA_n}{\sqrt{2}n\omega_s L} \tag{14}$$
$$I_{\text{peak}} \approx \sqrt{2}\,|I_P| \approx \sum_{n=1}^{\infty}\frac{\sqrt{B_n^2 + A_n^2}}{n\omega_s L}. \tag{15}$$

Define inductor current reference value $I_b$ and power reference value $P_b$ in (16) to facilitate normalized comparison of calculation results [13].

$$I_b = \frac{4}{\pi}\cdot\frac{\sqrt{3}V_m}{2\omega_s L} = \frac{2\sqrt{3}V_m}{\pi\omega_s L}$$
$$P_b = \frac{4}{\pi}\cdot\frac{\sqrt{3}NV_{\text{dc}}}{2}\cdot I_b = \frac{12V_m NV_{\text{dc}}}{\pi^2\omega_s L}. \tag{16}$$

The apparent power $S$ and active power $P$ in phasor form are as follows:

$$S = U_P I_P$$
$$P = \text{Re}(S) = \sum_{n=1}^{\infty}\frac{b_p(n)B_n - a_p(n)A_n}{2n\omega_s L}. \tag{17}$$

Finally, the normalized expressions for the active power $P_{\text{u}}$ and peak inductor current $I_{\text{u}}$ are as follows:

$$I_{\text{u}} = I_{\text{peak}}/I_b, P_{\text{u}} = P/P_b. \tag{18}$$

In the following analysis, we use the electrical parameters in Table II.

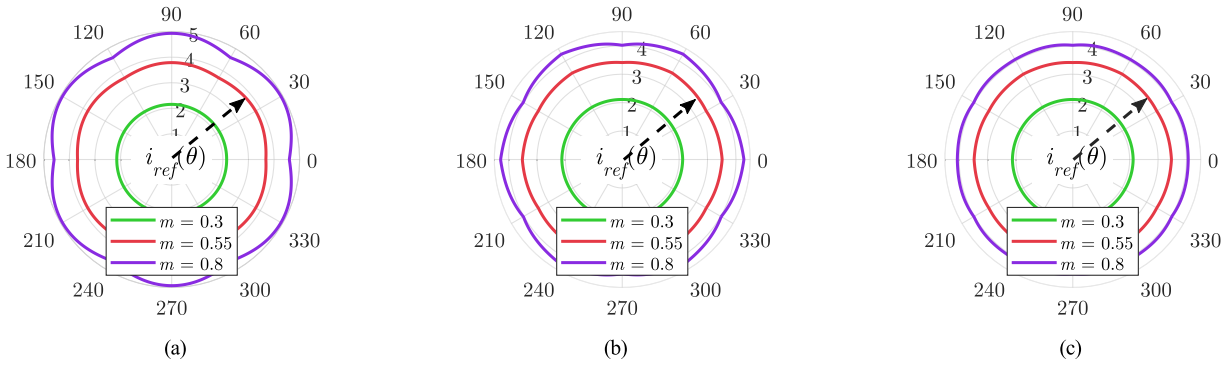


Fig. 6. Reference current vector curve (at $V_{dc} = 60$ V and $\phi_1 = 60°$). (a) Unoptimized. (b) After $m_1$ optimization. (c) After $m_1$ and $\phi_2$ optimization.

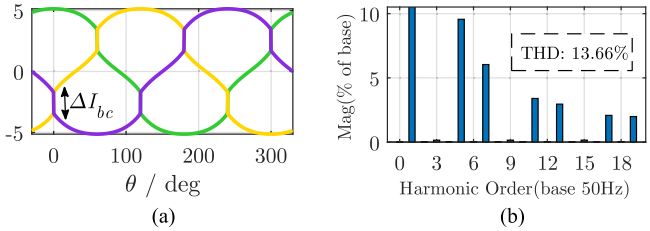


Fig. 7. Current distortion caused by DPS-SSVM before optimization. (a) Three-phase current. (b) THD harmonic analysis.

### D. Fourier Modeling of the Three-Phase Current

After filtering the high-frequency inductor current ($i_p$) through capacitors, the three-phase currents can be represented by the average switching period of the inductor current on the corresponding path. Refer to (19) for the relationship of current and the sum of three-phase current is zero.

$$\langle i_b\rangle_{Ts} = -\langle i_{ab}\rangle_{Ts} = \frac{-2}{T_s}\int_{t_2}^{t_3} i_p(t)dt$$
$$\langle i_c\rangle_{Ts} = -\langle i_{ac}\rangle_{Ts} = \frac{-2}{T_s}\int_{t_1}^{t_2} i_p(t)dt - \frac{2}{T_s}\int_{t_3}^{t_4} i_p(t)dt. \tag{19}$$

The current synthesis relationship is shown in (20), and the expression (21) for each phase current can be calculated from (19). Finally, the reference current polar coordinate diagram in Fig. 6(a) was plotted accordingly. The calculation results are consistent with the simulation. However, the unoptimized DPS-SSVM strategy introduces a large amount of harmonic content, especially the 5th and 7th harmonics, as shown in Fig. 7.

$$\vec{i}_{\text{ref}} = \frac{2}{3}\left(\langle i_a\rangle_{Ts} + \langle i_b\rangle_{Ts}e^{j\frac{2\pi}{3}} + \langle i_c\rangle_{Ts}e^{-j\frac{2\pi}{3}}\right). \tag{20}$$

By observing (10), (11), and (21), the absence of even-order harmonic components [as the Fourier coefficients $a_x(n)$ and $b_x(n)$ vanish for even $n$] and the fact that $\cos(n\pi/2)$ equals zero for all odd $n$, result in the correlation term $A_n\cos(n\pi/2)$ always being zero. As a direct result, the contribution of $A_n$ to (21) is null.

$$\begin{bmatrix}\langle i_a\rangle_{Ts}\\ \langle i_b\rangle_{Ts}\\ \langle i_c\rangle_{Ts}\end{bmatrix} = \frac{-2}{\pi\omega_s L}\sum_{n=1}^{\infty}\frac{1}{n^2}\left(A_n\cos\left(\frac{n\pi}{2}\right) + B_n\sin\left(\frac{n\pi}{2}\right)\right)$$
$$\cdot\begin{bmatrix}-\sin(\frac{n\pi}{2}m\cos\theta)\\ \sin(\frac{n\pi}{2}m\sin(\theta-\frac{\pi}{6}))\\ \sin\left(\frac{n\pi}{2}m\cos\theta\right)+\sin\left(\frac{n\pi}{2}m\sin\left(\frac{\pi}{6}-\theta\right)\right)\end{bmatrix}. \tag{21}$$

Consequently, only $A_n$ depends on the power angle ($\varphi$). This demonstrates the independence and decoupling between $\varphi$ and the analytical model for the three-phase current (21). Therefore, the analytical expression for the three-phase current holds for any PF, implying that adjusting the system's PF does not affect its sinusoidal characteristics. Thus, we have theoretically proven that the THD optimization method based on (21), proposed in the next part, is consistently effective for the three-phase currents at any PF.

### E. Optimization Process of Distorted Current

HFLMC is suitable for distributed new energy scenarios such as household PV and energy storage, and EV charging. To fundamentally address the issue of three-phase current distortion, this study introduces targeted optimization techniques based on dual vector modulation indices ($m_1$ and $m_2$) and dual phase-shift coordination.

To explain this optimization approach, consider the distorted currents shown in Fig. 7. At 0°, the B-phase and C-phase currents should be equal to satisfy sinusoidal characteristics. However, according to (21), a single modulation index $m$ cannot satisfy this condition. Therefore, this work proposes the introduction of additional modulation indices to independently control the current vector inputs. This enables control of the current amplitudes and ensures that the theoretical model conforms to sinusoidal characteristics. Modulation indices ($m_1$ *and* $m_2$) directly control the current amplitude by governing the utilization rate and conduction duration of their associated current vectors, maintaining their phase angle relationship with time.

To explore the relationship between physical phenomena and mathematical modeling, $m_1$ and $m_2$ are represented by the parameters $T_1$ and $T_2$, respectively. However, the introduction of $T_1$ and $T_2$ as variables only affects the Fourier coefficient $b_p(n)$

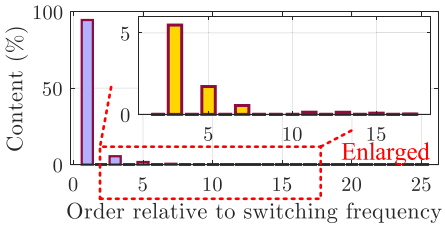


Fig. 8. The proportion of each component of the switching frequency in the Fourier series of three-phase current.

TABLE III
MULTIVARIABLE COORDINATED MODULATION FUNCTION

| Definition | Variables definition of modulation function | | |
|---|---|---|---|
| **Input parameters (Independent)** | Primary Phase-shift angle $\phi_1$ | Vector modulation index $m$ | Sub vector modulation index $m_2 = m$ |
| **Time-varying parameter** | Phase angle of three-phase reference current $\theta$ | | |
| **Output parameters (Dependent)** | Main vector modulation index $m_1(\phi_1, m)$ | The maximum value of the secondary phase-shift angle $\phi_{2\max}(\phi_1, m)$ | Secondary Phase-shift angle $\phi_2(\phi_{2\max}, \theta)$ |

in the series expansion, which resides within the unrelated $A_n$ term. Consequently, by adjusting the upper and lower limits of the integral in (19) to incorporate the variables $m_1$ and $m_2$, we derive the Fourier series expressions for the three-phase current in (22) —specifically, the closed-form solutions for individual harmonic components—with corresponding amplitude ratios depicted in Fig. 8.

Furthermore, Fast Fourier Transform (FFT) analysis of the calculation data (see Fig. 8) reveals that the harmonic proportion at switching frequencies of the 7th order and above is less than 1%. Thus, in subsequent calculations, only the 1st, 3rd, and 5th switching frequency components are included for equivalent approximation.

$$
\begin{aligned}
i_a(n,\theta) &= C_n \sin\left(\frac{n\pi}{2}\left[m_1 \sin\left(\frac{\pi}{6}-\theta\right)+m_2 \sin\left(\frac{\pi}{6}+\theta\right)\right]\right)\\
i_b(n,\theta) &= -C_n \sin\left(\frac{n\pi}{2} m_1 \sin\left(\frac{\pi}{6}-\theta\right)\right)\\
i_a(n,\theta) &+ i_b(n,\theta) + i_c(n,\theta) = 0
\end{aligned}
\tag{22}
$$

where $C_n$ is the current amplitude coefficient composed only of dc voltage and two phase-shift angles, expressed as follows:

$$
C_n = \frac{4NV_{\text{dc}}\left\{\sin(n\phi_1)[1+\cos(n\phi_2)]-\sin^2(n\phi_2)\right\}}{\csc(n\pi/2)\cdot n^3\pi^2\omega_s L}. \tag{23}
$$

In order to correct the three-phase current modulated by DPS-SSVM to a standard sine curve, a multivariable coordinated modulation function was first defined, with the variables of this modulation function presented in Table III. The ultimate goal of this modulation function is to minimize THD as much as possible.

The input parameters characterize the modulation state of the circuit and directly determine the system's operating point. Time-varying parameters also influence the output of the dependent variables. Using (22) as the analysis basis, this study combines the following three mathematical conditions to eliminate the three-phase current THD.

1) *Condition 1:* When $\theta = 0$, make the currents of B-phase and C-phase equal to reduce the 5th and 7th harmonics.

$$
\sum_{n=1,3,5}^{\infty} i_b(n,\theta=0) = \sum_{n=1,3,5}^{\infty} i_c(n,\theta=0) \tag{24}
$$

From Fig. 7, it can be observed that the currents in phases B and C are not equal at 0°. The $C_n$ is affected by two phase-shift angles, where the secondary phase angle ($\phi_2$) is the internal phase angle used by the H-bridge to generate zero level, leading to a current circulation problem that reduces efficiency. In addition, increasing $\phi_2$ extends the duration of the zero level, which only reduces $C_n$ and lowers the power output. The output power in (17) can be adjusted by two variables that have a greater impact, $m$ and $\phi_1$. In summary, to improve efficiency without reducing transmission power, the range of variation of $\phi_2$ should be minimized. Therefore, $\phi_2$ plays only an auxiliary role in correcting current THD. Consequently, the above conditional equation can be simplified, considering the subsequent calculation results, and $\phi_2$ can be set to a smaller average value (10°).

Solving (24) yields, and the result is shown in Fig. 9(a). The calculation formula for the surface after polynomial fitting is provided in Appendix (A1). By substituting the dual modulation indices results from (A1), the polar coordinates of the three-phase output current amplitude under the DPS-SSVM strategy are illustrated in Fig. 6(b). However, the amplitude of the synthesized reference current vector still does not form a standard circle, as its amplitude varies periodically every two sectors (60°) and exhibits symmetry. Therefore, the optimization approach for Condition 2 involves using the minimum current amplitude within each sector as a baseline and reducing excessive amplitude by adjusting the modulation variable (the secondary phase-shift angle, $\phi_2$).

2) *Condition 2:* Increase the secondary phase-shift angle when the amplitude of the reference current vector is large to weaken the amplitude and shape the reference current vector into a standard circle.

Taking the 12th sector as an example, the secondary phase-shift angle should be set to 0 at the beginning of the interval and reach its maximum value at the end of the interval. The maximum value is directly determined by input parameters. For the A-phase current, the following trigonometric relationship (25) must be satisfied:

$$
\begin{aligned}
&\sum_{n=1,3,5}^{\infty} i_a\left(n,\theta=-\frac{\pi}{6},\phi_2=0\right)\\
&= \cos\left(-\frac{\pi}{6}\right)\cdot\left(\sum_{n=1,3,5}^{\infty} i_a(n,\theta=0,\phi_2=\phi_{2\max})\right).
\end{aligned}
\tag{25}
$$

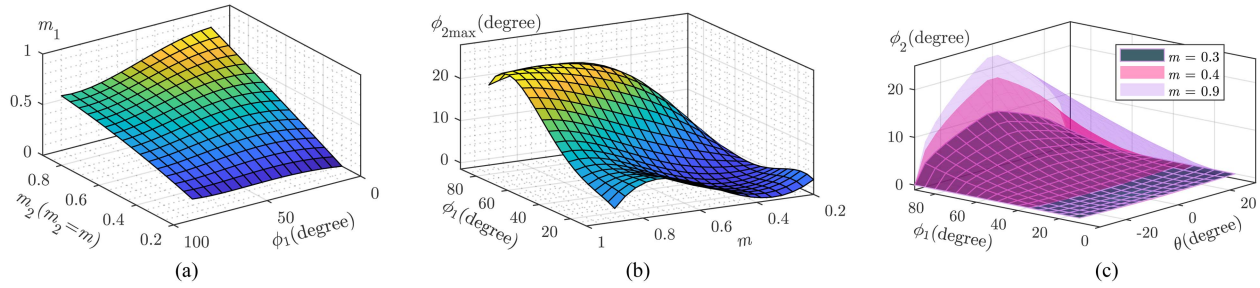


Fig. 9. Variable relationships in modulation functions. (a) The first condition output. (b) The second condition output. (c) The third condition output.

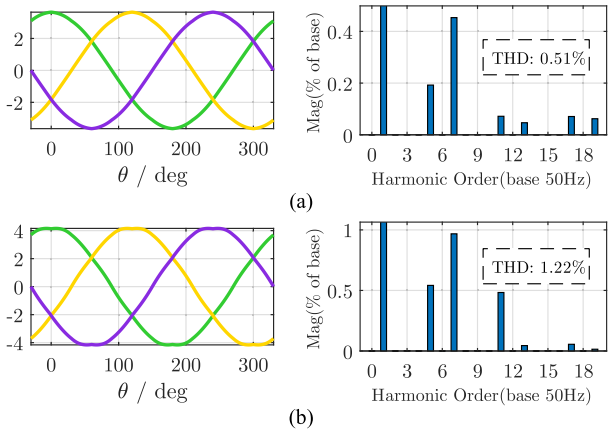


Fig. 10. Simulation results of three-phase current after optimization. (a) $m = 0.6$, $\phi_1 = -60°$. (b) $m = 0.8$, $\phi_1 = -90°$.

Solving for the surface ($\phi_{2\max}(\phi_1, m)$) from (25) leads to the result shown in Fig. 9(b). The approximate calculation formula is provided in Appendix (A2).

3) Condition 3: With a constant synthesized current amplitude as the objective, calculate the curve of $\phi_2$ with respect to the phase angle $\theta$ using a simple function.

The secondary phase-shift angle is a variable influenced by a time-varying parameter ($\theta$). Ensure that $\phi_2$ starts at 0 at the beginning of the interval and reaches its maximum value at 0°. A simple square root function in (26) satisfies this requirement, and the final calculation result is shown in Fig. 6(c), where the synthesized reference current closely approximates a standard circle.

$$\phi_2(\phi_{2\max}(m,\phi_1),\theta) = \phi_{2\max}(m,\phi_1)\cdot(1-6\,|\theta|/\pi)^{1/2}. \tag{26}$$

### F. Simulation and Verification

Following the theoretical optimization strategies outlined, this section employs the optimized modulation function for simulation verification to evaluate the THD performance of the proposed method in this article.

Fig. 10 shows the current waveforms and THD simulation results obtained after optimization. Fig. 11 illustrates the statistical THD outcomes of the DPS-SSVM strategy before and after optimization across various input parameters. The results indicate that within the range of $m$ from 0.3 to 0.8 and $\phi_1$ from 30° to 90°, the average THD decreased by 3.4%, achieving an optimized value of 1.22%, with the maximum reduction reaching 11.3%.

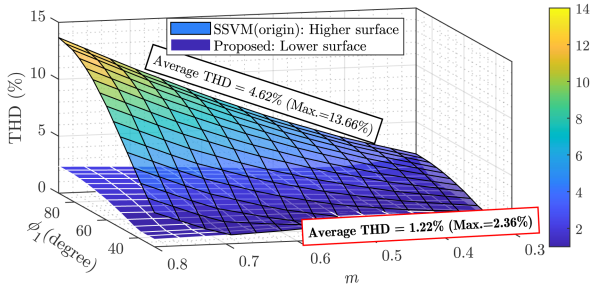


Fig. 11. Statistical surface of current THD before and after optimization.

## III. Comparative Analysis of Performance

### A. Modeling of Existing Mainstream Modulation Strategies

The modulation strategy proposed in this study demonstrates strong performance across various aspects. For comparative analysis, three strategies for the primary voltage have been selected here which are labeled as SVM1 [4], [5], [18], SVM2 [20], and SVM3 [13]. The key waveforms for each method at the 12th sector are illustrated in Fig. 12.

The current vector relationships of these three SVM strategies follow the vector synthesis rule (6), and utilize the same modulation index $m$. The timing relationships for SVM1 and SVM2 are defined in (27) and (28), respectively. SVM3 modifies the zero vectors of SVM2 to address the THD issue, as shown in (29) [13]. The common point of these methods is that it is difficult to solve the exact three-phase current analytic formula in the time domain, because the primary voltage is time-varying and the phase-shift angle is undetermined.

$$\begin{cases} T_{1(\mathrm{SVM1})} = 2\cdot(t_1-t_0) = 2\cdot(t_4-t_3) \\ T_{2(\mathrm{SVM1})} = 2\cdot(t_2-t_1) = 2\cdot(t_5-t_4) \end{cases} \tag{27}$$

$$\begin{cases} T_{1(\mathrm{SVM2})} = 2\cdot(t_1-t_0) = 2\cdot(t_5-t_4) \\ T_{2(\mathrm{SVM2})} = 2\cdot(t_2-t_1) = 2\cdot(t_4-t_3) \end{cases} \tag{28}$$

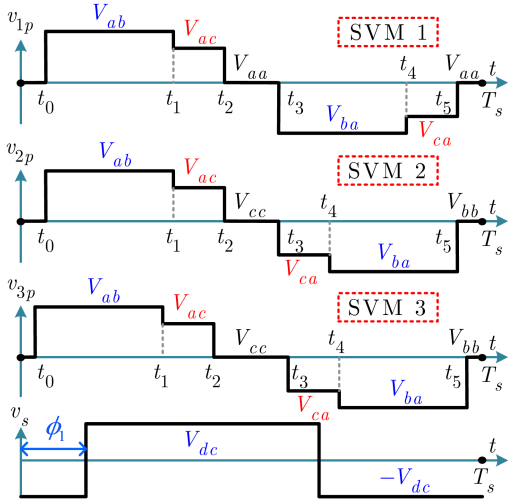


Fig. 12. Several mainstream SVM modulation strategies.

$$\begin{cases} T_{1(\text{SVM3})} = 2\cdot(t_1-t_0) = 2\cdot(t_5-t_4) \\ T_{2(\text{SVM3})} = 2\cdot(t_2-t_1) = 2\cdot(t_4-t_3) \\ T_{01(\text{SVM3})} = (T_s-t_5+t_0) = T_s\left(\frac{1}{2}+\frac{m}{\sqrt{3}}\sin(\theta-\frac{\pi}{3})\right)\cdot \\ T_{02(\text{SVM3})} = (t_3-t_2) = T_s\left(\frac{1}{2}-\frac{m}{\sqrt{3}}\sin(\theta+\frac{\pi}{3})\right) \end{cases} \tag{29}$$

Using Fourier series expansion, these three SVM modulation strategies can be analyzed consistently. Taking SVM1 as an example, the calculation process begins with determining certain variables in the HFT, as outlined in (30). The Fourier coefficients are directly derived using the definition formula in (31).

For the secondary voltage, the Fourier coefficients in (32) are obtained by setting the secondary phase-shift angle to zero in (10). The current series in the time domain is represented by (33).

$$\begin{aligned} v_{1p}(t) &= \sum_{n=1,2,3}^{\infty}\left[a_{1p}(n)\cos(n\omega_s t)+b_{1p}(n)\sin(n\omega_s t)\right] \\ v_{1s}(t) &= \sum_{n=1,2,3}^{\infty} a_{1s}(n)\cos(n\omega_s t-n\phi_1) \\ &\quad+\sum_{n=1,2,3}^{\infty} b_{1s}(n)\sin(n\omega_s t-n\phi_1) \end{aligned} \tag{30}$$

$$\begin{aligned} a_{1p}(n) &= \frac{2}{T_s}\left[\int_{t_0}^{t_1} V_{ab}\cos(n\omega_s t)dt+\int_{t_1}^{t_2} V_{ac}\cos(n\omega_s t)dt\right. \\ &\quad\left.+\int_{t_3}^{t_4} V_{ba}\cos(n\omega_s t)dt+\int_{t_4}^{t_5} V_{ca}\cos(n\omega_s t)dt\right] \\ b_{1p}(n) &= \frac{2}{T_s}\left[\int_{t_0}^{t_1} V_{ab}\sin(n\omega_s t)dt+\int_{t_1}^{t_2} V_{ac}\sin(n\omega_s t)dt\right. \\ &\quad\left.+\int_{t_3}^{t_4} V_{ba}\sin(n\omega_s t)dt+\int_{t_4}^{t_5} V_{ca}\sin(n\omega_s t)dt\right] \end{aligned} \tag{31}$$

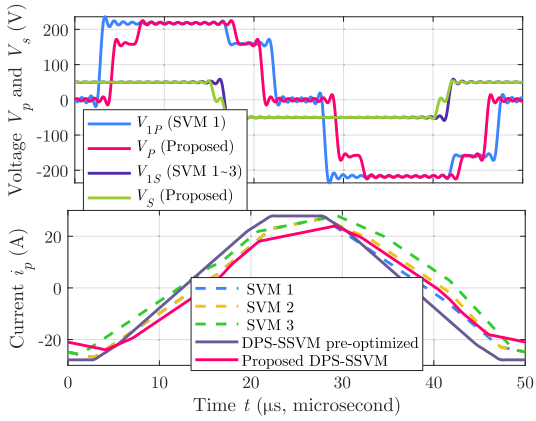


Fig. 13. The calculation results of HFT voltage and current, under $m = 0.8$ and primary phase-shift angle =-60°.

$$\begin{bmatrix} a_{1s}(n) \\ b_{1s}(n) \end{bmatrix} = \frac{2V_{dc}}{n\pi}\begin{bmatrix} \sin(n\pi) \\ 1-\cos(n\pi) \end{bmatrix} = \frac{4V_{dc}}{n\pi}\begin{bmatrix} 0 \\ 1 \end{bmatrix}, n = 1,3,5, \tag{32}$$

$$\begin{aligned} i_{1p}(t) &= \frac{1}{\omega_s L}\sum_{n=1}^{\infty}\frac{1}{n}\left[A_{1n}\cos(n\omega_s t)+B_{1n}\sin(n\omega_s t)\right] \\ \begin{bmatrix} A_{1n} \\ B_{1n} \end{bmatrix} &= N\begin{bmatrix} a_{1s}(n) & b_{1s}(n) \\ b_{1s}(n) & -a_{1s}(n) \end{bmatrix}\cdot\begin{bmatrix} \sin(n\phi_1) \\ \cos(n\phi_1) \end{bmatrix} \\ &\quad+\begin{bmatrix} -b_{1p}(n) \\ a_{1p}(n) \end{bmatrix}. \end{aligned} \tag{33}$$

Finally, the expressions for active and inductor peak currents in phasor form, as shown in (34), are used to calculate the normalization results.

$$\begin{aligned} P_1 &= \sum_{n=1}^{\infty}\frac{b_{1p}(n)B_{1n}-a_{1p}(n)A_{1n}}{2n\omega_s L}, \\ I_{1\text{peak}} &\approx \sum_{n=1}^{\infty}\frac{\sqrt{B_{1n}^2+A_{1n}^2}}{n\omega_s L}. \end{aligned} \tag{34}$$

Referring to Table II, the parameters for each SVM strategy and the proposed strategy are calculated, with the proposed strategy labeled as "Proposed" post-optimization and "DPS-SSVM(pre)" preoptimization. To demonstrate the Fourier series approximation principle, fifty times switching frequencies were superimposed, and the results are presented in Fig. 13.

### B. Suppression of Peak Inductance Current

Following the verification of the calculation results, a performance comparison analysis is conducted based on the developed models.

Fig. 14 shows that the normalized maximum power points of other modulation strategies are around 1, while SVM1, due to its unique sorting method, has a nonzero $a_{1p}(n)$ coefficient and can carry greater power during the switching period. In contrast, due to the secondary phase-shift angle and a smaller main vector modulation index in DPS-SSVM, the peak power slightly decreases, achieving a normalized value of 0.852. In

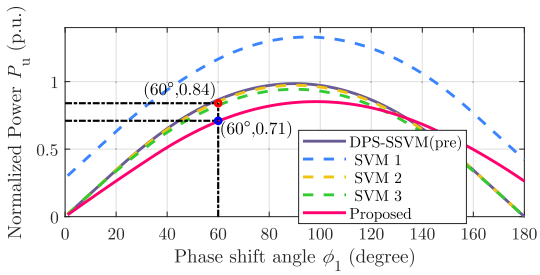


Fig. 14. The relationship between normalized output power and primary phase-shift angle at $m = 0.8$.

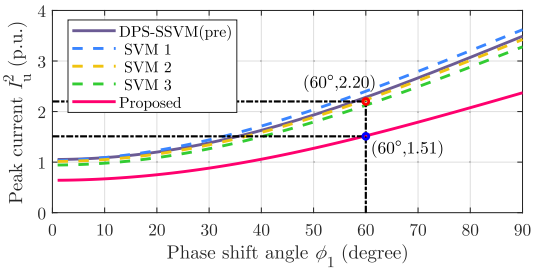


Fig. 15. The relationship between normalized peak current (squared) of inductor and the first phase-shift angle (when $m = 0.8$).

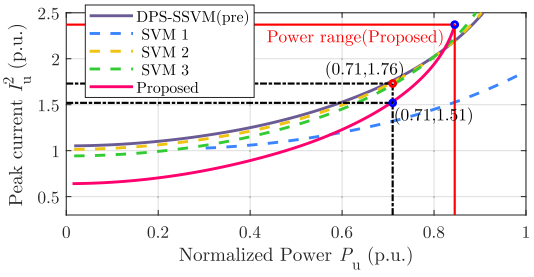


Fig. 16. The relationship between normalized peak current (squared) of inductor and normalized output power (when $m = 0.8$).

addition, the maximum power point of the primary phase-shift angle shifts from 90° to 96° (the offset angle is half of the additional secondary phase-shift angle). At primary phase-shift angle of 60°, the output power decreases to about 85% of the preoptimization level compared to DPS-SSVM (pre).

Fig. 15 demonstrates that the proposed strategy in this article results in lower current stress at the same phase-shift angle, with current stress at 60° being approximately 69% of that observed in other methods. Furthermore, Fig. 16 shows that the DPS-SSVM optimization method achieves a normalized power range from 0 to 0.852. The calculation results indicate that when the normalized power ($P_u$) is below 0.8, the peak inductance current of the proposed strategy is the smallest, particularly at light loads where peak current suppression is more pronounced. For instance, at $P_u = 0.71$, the peak current of the proposed method is about 85.7% of that of SVM2,3 methods, and at $P_u = 0.3$, it is reduced to 69%. After $P_u$>0.6, the peak current of SVM1 is lower, but its THD is really poor (as discussed below).

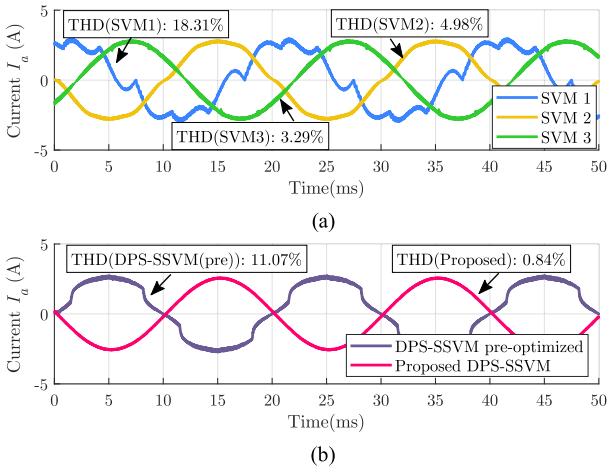


Fig. 17. The simulation results of A-phase current for different SVM strategies ($m = 0.8$, Primary phase-shift angle=-60°). (a) SVM1 (The value is divided by 4 to facilitate the display of the waveform), SVM2 and SVM3. (b) DPS-SSVM method before and after optimization.

### C. Performance Metrics: Current THD, DC-Bias, and Low-Frequency Current Ripple

*1) THD Performance:* Verification through Matlab/Simulink simulation provides a comprehensive analysis of A-phase current, focusing on THD, as shown in Fig. 17. The simulation results indicate THD values of 18.31% for SVM1, 4.98% for SVM2, 3.29% for SVM3, with the DPS-SSVM strategy showing 11.07% before optimization and significantly reducing to 0.84%.

*2) Reduction of DC-Bias and Current Ripple:* Beyond THD, the reduction of dc-bias and current ripple is another critical aspect of performance. Given that the three-phase voltage cannot be assumed constant over a short switching cycle, the changing line voltage in (35) impacts the volt–second balance of the transformer, leading to varied dc-bias levels across different strategies [22].

$$V_p = \begin{cases} \pm v_{ab} = \pm\sqrt{3}V_m \cos(\omega(t+\Delta t)+\pi/6) \\ \pm v_{ac} = \pm\sqrt{3}V_m \cos(\omega(t+\Delta t)-\pi/6) \end{cases}. \quad (35)$$

This imbalance in voltage across the power inductor results in an offset of inductor current (which cannot reset within one cycle), causing significant fluctuations in the three-phase voltage cycle, as illustrated in Fig. 18.

When assessing dc-bias, the variable $\Delta S_{dc}$ defined in (36) represents the integral sum of primary voltage over each switching cycle, correlating directly with the slope of the dc-bias current: This analysis demonstrates that the proposed DPS-SSVM strategy not only excels in reducing THD, but also effectively minimizes dc-bias and current ripple, ensuring a more stable and efficient operation across different load conditions.

$$\triangle S_{dc} = \int_{-T_S/2}^{T_S/2} v_p(t)dt. \quad (36)$$

Based on (35) and (36), calculations of the volt–second integration for different strategies are shown in Fig. 19. Notably,

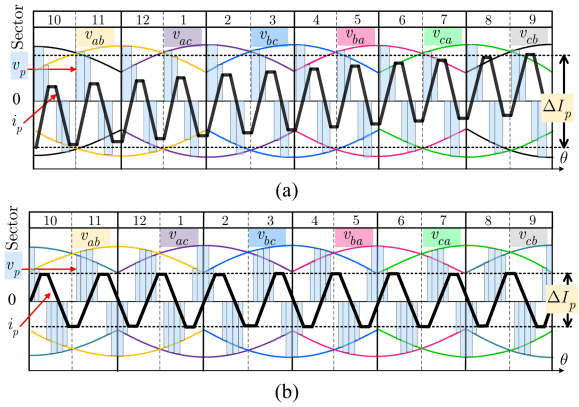


Fig. 18. Schematic diagram of DC-bias problem caused by volt-second imbalance in inductor current. (a) The situation where the volt-second integral is always positive (b) The situation where the volt-second integral maintains zero axis balance.

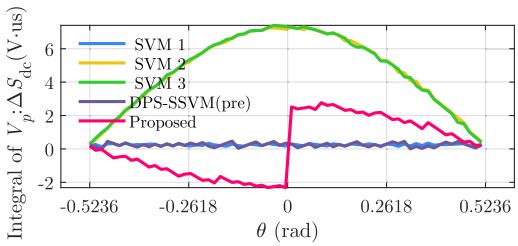


Fig. 19. Integration result of the primary voltage in sectors 12 to 1.

the dc-bias for SVM1 and the unoptimized strategy in this article (SSVM) can be considered negligible, while for SVM2 and SVM3, the remains consistently positive. The optimized DPS-SSVM strategy presents a balanced approach where the integral first dips negative then rises positive, averaging at zero. The maximum amplitude here is only one-third of that seen in SVM2 and SVM3.

This approach nearly guarantees a dynamic balance in volt–seconds over a 60° period, effectively reducing dc-bias and minimizing low-frequency current ripple. Integrating the $\Delta S_{dc}$ over a 60° interval (3.33 ms), the integration results for SVM1 to SVM3 are 0.1649, 3.1604, and 3.1542, respectively, while the results before and after optimization for the method in this article are 0.1619 and 0.1041, measured in V·$\mu$s·rad.

### D. Reduction of CMV

CMV significantly impacts the electromagnetic compatibility performance of converters. Numerous studies have addressed the CMV issues in three-phase inverters and HFLMCs [22], [27]. The definition of CMV is provided as follows:

$$V_{\mathrm{CMV}} = \frac{1}{2}\left[(v_{\mathrm{up}} - v_{\mathrm{o}}) + (v_{\mathrm{dn}} - v_{\mathrm{o}})\right] = \frac{1}{2}(v_{\mathrm{up_o}} + v_{\mathrm{dn_o}}). \quad (37)$$

Within the phase angle range of the 12th sector, the possible values of CMV are simplified as shown in (38), the first two levels correspond to the CMV generated by the main and sub vectors, while the last three levels correspond to the CMV

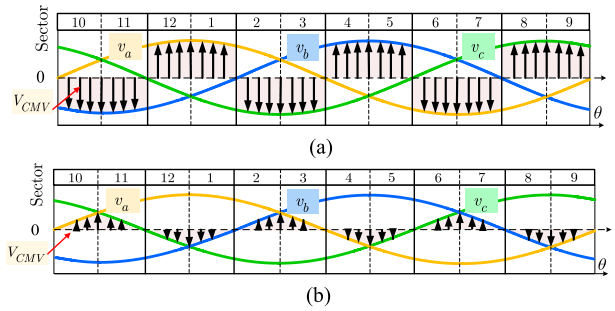


Fig. 20. Schematic diagram of CMV amplitude introduced by different SVM strategies. (a) SVM1 and [11], [18], [19], [22], [25], [26]. (b) SVM2, SVM3, [13], [20], [22], [27] and this paper.

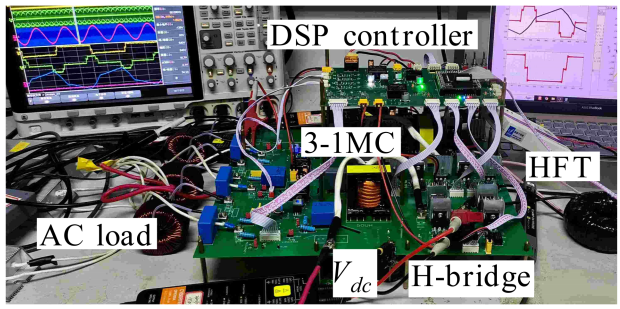


Fig. 21. Experimental platform.

produced by the three zero vectors

$$|V_{\mathrm{CMV}}| = \frac{1}{2}\begin{cases} |v_a + v_b| < \sqrt{3}V_m/4 \\ |v_a + v_c| < \sqrt{3}V_m/4 \\ |v_a + v_a| \in [0.5V_m, V_m] \\ |v_b + v_b| < 0.5V_m \\ |v_c + v_c| < 0.5V_m \end{cases}. \quad (38)$$

Clearly, the CMV amplitude associated with the main and sub vectors is smaller. The CMV of the zero vector $I_7(V_{aa})$ is twice that of the other zero vectors. Therefore, when calculating the CMV amplitude for different strategies, only the selection of their zero vectors needs to be considered. According to the statistical data, the CMV amplitude caused by various strategies is indicated by the black arrow in Fig. 20. The proposed method introduces a CMV that is only 50% of the phase voltage amplitude, demonstrating superior performance.

## IV. Comparative Experimental Verification

### A. Statistics of Total Harmonic Content (THD) of Current

To validate the effectiveness of the proposed strategy, an experimental prototype of a three-phase approximately 110 V (RMS)/48 Ω/50 Hz HFLMC was constructed, as shown in Fig. 21. The system operates in inverter mode using IGBTs and the parameters are listed in Table II. A single DSP was employed to manage the modulation process. The parameters received by DSP are: index $m$, the first phase-shift angle, and other parameters can be initialized through equations.

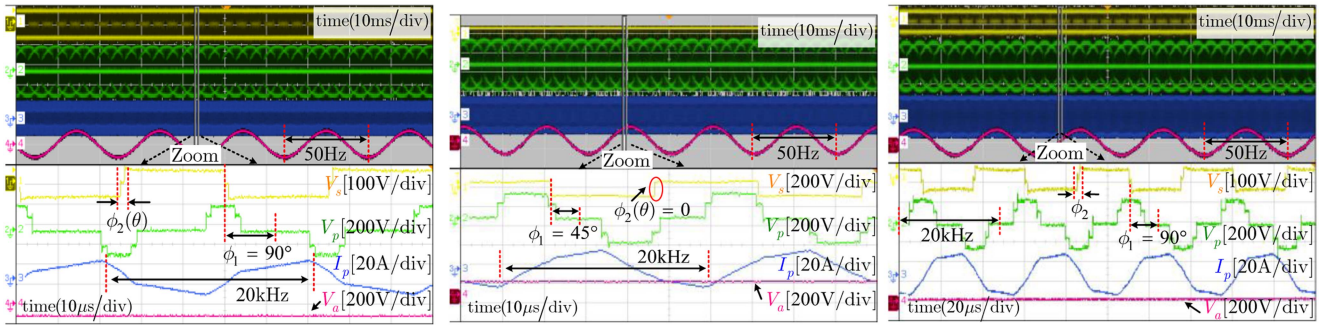


Fig. 22. Proposed DPS-SSVM experimental results at three-phase $V_m$ = 140±5 V/48 Ω/50 Hz. (a) $m$=0.4 and Primary phase-shift angle=-90°. (b) $m$ =0.6 and Primary phase-shift angle=-45°. (c) $m$ =0.8 and Primary phase-shift angle=-90°.

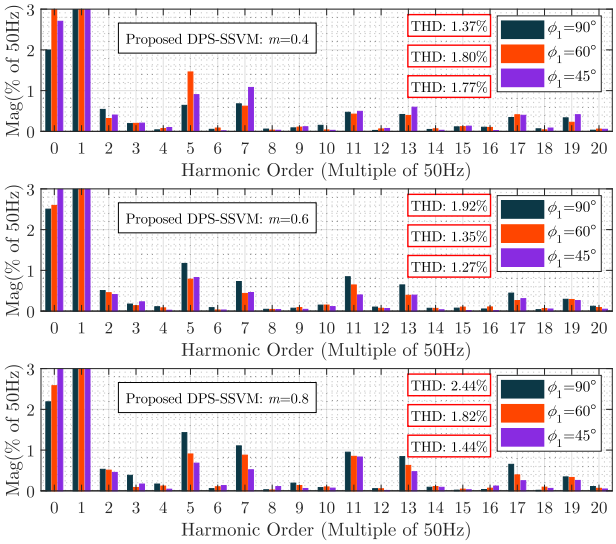


Fig. 23. FFT analysis of A-phase voltage in inverter experiment under 9 groups of input parameter combinations.

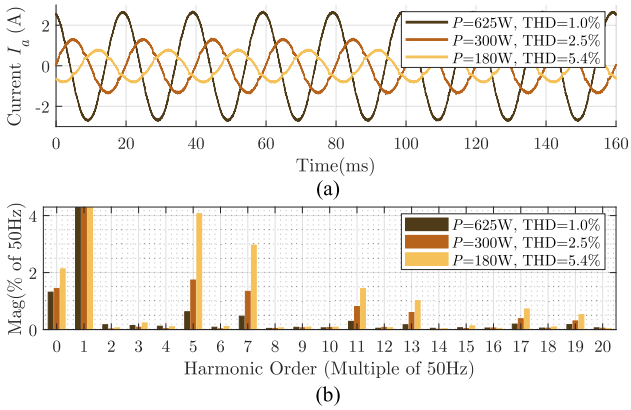


Fig. 24. Variable load test of three-phase 100 Vrms inverter experiment under 48 Ω × 3, 96 Ω × 3 and 167 Ω × 3. (a) Experimental data of A-phase current. (b) FFT analysis of experimental data of A-phase current.

Fig. 22 presents the experimental results under various input parameters, specifically modulation index $m$ and primary phase-shift angle. Subsequently, Fig. 23 displays the FFT analysis and statistics of A-phase voltage waveforms across nine different input parameter combinations: $m$(0.4, 0.6, 0.8) × $\phi_1(-45°, -60°, -90°)$ in inverter mode, which is carried out at the rated power of 800 W. The average THD observed across these nine working points is 1.687%, demonstrating the effectiveness of the proposed strategy in reducing harmonic distortion. In addition, we also tested the A-phase current and FFT analysis under the same output voltage (100 Vrms) and different loads, as shown in Fig. 24. For the 2% zero order component, the main reasons are: the parameters of the three-phase high-frequency filter capacitor are not strictly symmetrical, with ESR, and the load resistance is asymmetric. In addition, the difference in the propagation delay of the drive circuit (ns level) may lead to inconsistent dead time.

### B. Comparison of Current of Inductors

For further experimental verification, this article compares the proposed DPS-SSVM strategy with two other well-regarded modulation strategies, SVM2 (known for improved THD) and SVM3 (further enhanced according to [13]). Under identical input parameters and load conditions, the experimental results are presented in Fig. 25.

In this comparison, considering low-frequency current ripple, the peak-to-peak current across a three-phase cycle for SVM2 was 55 A, for SVM3 it was 60 A, whereas the DPS-SSVM strategy only reached 43 A, showing no pulsation. At the smaller scale of switching cycles, the peak-to-peak currents for SVM2, SVM3, and DPS-SSVM were 48 A, 47 A, and 40 A, respectively.

The peak current at the switching cycle scale for the proposed DPS-SSVM is approximately 84% of the other strategies, aligning with theoretical expectations. Moreover, due to the effective elimination of dc-bias, the peak value over the three-phase periodic scale is reduced to between 72% and 78% of SVM2 and SVM3. Hence, regardless of whether considering the scale of switching cycles or three-phase cycles, compared to the improved method SVM2 and SVM3, the method proposed herein consistently achieves the lowest current peaks.

### C. Performance Metrics: CMV Test Results, THD, Efficiency, and Number of Controllers

*1) CMV Test:* The experimental results in Fig. 26 prove that the DPS-SSVM strategy avoids the application of high amplitude zero vector, thus reducing the CMV amplitude to half of the phase voltage amplitude. Compared with the traditional

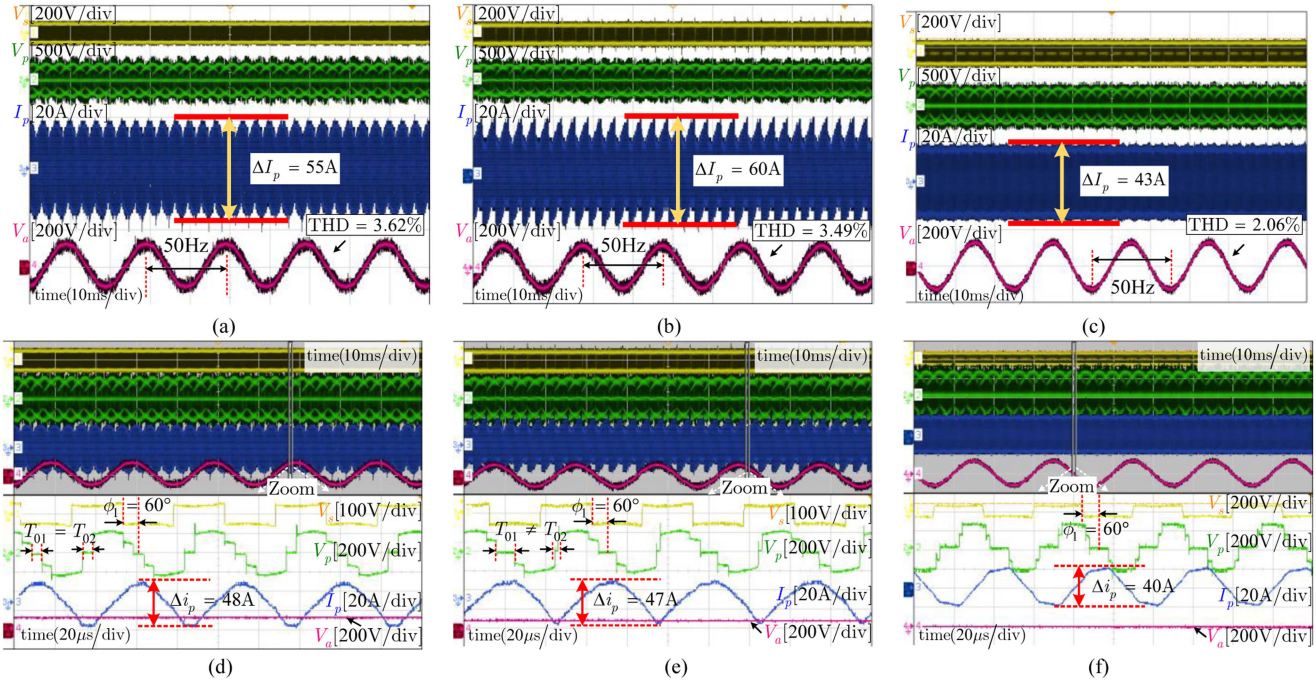


Fig. 25. Output waveforms of different strategies under input parameters ($m$ =0.8 and Primary phase-shift angle =−60°) at three-phase $V_m$ = 130±5 V/48 Ω/50 Hz. (a) SVM2 low-frequency scale. (b) SVM3 low-frequency scale. (c) DPS-SSVM low-frequency scale. (d) SVM2 high-frequency scale. (e) SVM3 high-frequency scale. (f) DPS-SSVM high-frequency scale.

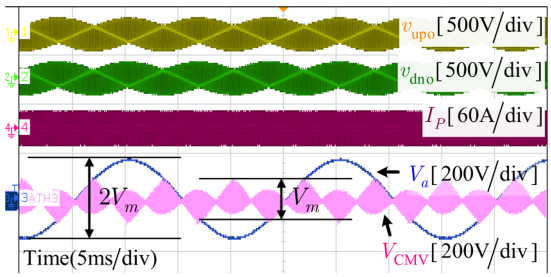


Fig. 26. Common mode voltage test results (at about 120 Vrms, 900 W).

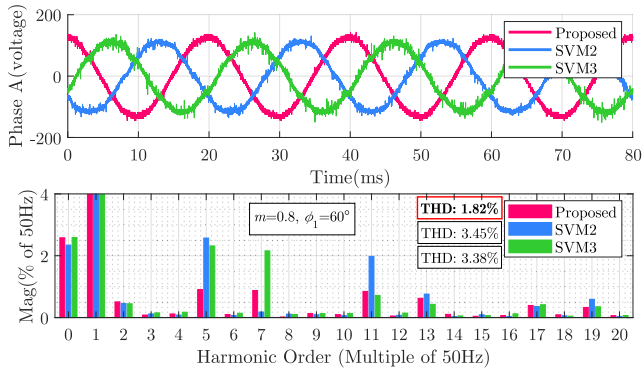


Fig. 27. THD comparison of A-phase voltage experimental data.

TABLE IV
EXPERIMENTAL THD COMPARISON

| Current THD | Modulation methods of HFLMC |
|---|---|
| >8% | [12, 14] |
| 5%~8% | [23] |
| 3%~5% | [10, 13, 18, 20, 26] |
| 2%~3% | [11, 15, 25, 27] |
| 1.687% | This paper |

TABLE V
COMPARISON OF CONTROLLER QUANTITY

| Controller platform | Modulation methods of HFLMC |
|---|---|
| DSP+FPGA | [11–15, 17, 18, 20, 25, 26] |
| Only 1 DSP | [23, 27] and this paper |

strategy, the SSVM strategy can avoid using the zero vector with larger common mode amplitude [22].

*2) THD Performance:* Fig. 27 presents the FFT analysis of the A-phase voltage experimental data, showing that even among strategies optimized for THD, the DPS-SSVM proposed here, based on an optimized modulation function, achieve notably lower THD even in an open-loop scenario. When compared against the experimental results of other strategies listed in Table IV, the average THD from DPS-SSVM experiments is only 1.687% (Wide range modulation parameters at rated power).

*3) Efficiency:* The efficiency of the three modulation strategies is measured on the same IGBT-based experimental prototype with the same parameters, and the results are shown in Fig. 28. The observed improvement in system efficiency may be a beneficial by-product of the proposed THD optimization strategy. Reducing harmonic distortion usually helps to reduce

TABLE VI
PERFORMANCE SUMMARY OF DIFFERENT MODULATION STRATEGIES FOR HFLMC TOPOLOGY

| **Performance** | **Experimental results on the same IGBT-based theoretical verification platform** | | | **Conventional modulation strategies and the conclusions given in the references** | | |
|---|---|---|---|---|---|---|
| Modulation strategies | **Proposed** (DPS-SSVM) | Optimized type (SVM2) | THD improved type (SVM3) in [13] | Conventional type (SVM1) | Method in [11] | Method in [6] |
| Peak value of current low frequency fluctuation (normalized) | **72%** | 92% | 100% | / | / | / |
| Peak value of high frequency current (normalized) | **84%** | 100% | 98% | 92% | / | / |
| Narrow pulses (<3% $T_s$) content (Calculation results) | 8% | **6%** | 10.1% | 37.7% | 17.6% | / |
| The number of switching actions per cycle | 12 | **10** | **10** | **10** | 18 | 23 |
| THD performance | **~2%** | 3.62% | 3.49% | >15% | 2~3% | ~2% |
| Common mode voltage amplitude (normalized) | **50%** | **50%** | **50%** | 100% | 100% | 100% |
| Efficiency | **81%**@510W | 78%@510W | 77%@510W | / | / | **81%**@825W |

The bolded entities indicate the best results in their respective rows.

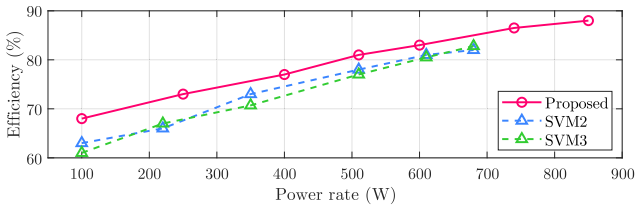


Fig. 28. Efficiency estimation of different strategies under the same experimental prototype.

conduction losses and harmonic related losses in power components. In addition, the calculation results of (15) and Fig. 16 together with the experiment (see Fig. 25) prove that DPS-SSVM can effectively reduce the peak and RMS current, and maintain a good magnetic balance effect. It can be observed from Fig. 25 that the waveform of DPS-SSVM reduces high-frequency noise, reflecting the reduction of switching loss to a certain extent. These improvements are helpful to reduce the copper loss and magnetic loss of the circuit conduction.

*4) The Number of Control Chips in the Controller:* Despite the complexity involved in implementing the DPS-SSVM strategy, the experimental setup utilized only a single DSP chip (TMS320F28377D). This is a significant advantage compared to other methods, as detailed in Table V. The SSVM layout can be efficiently implemented in a DSP using up–down counting mode comparators, enabling precise current commutation with just one DSP. In contrast to other studies, this approach eliminates the need for an additional FPGA module, thereby substantially reducing control costs and simplifying the overall system architecture.

## V. CONCLUSION

This study introduced a DPS-SSVM strategy utilizing FDA to optimize THD through dual modulation indices. The overall experimental comparison is shown in Table VI.

By developing a FDA model with Fourier transforms, we effectively addressed the complexities associated with TDA, enhancing the universality and adaptability of HFLMC modulation models. The proposed DPS-SSVM strategy, which incorporates dual modulation indices and dual phase-shift angles, successfully mitigates the dc-bias issues inherent in traditional modulation methods. This leads to significant reductions in current stress and ripple, elimination of narrow pulses, and balanced dc-bias. Experimental validation was conducted using a three-phase 800 W HFLMC prototype, demonstrating that DPS-SSVM achieves an average THD of 1.687%, lowers peak inductance currents to 84% on the switching cycle scale and 72-78% on the grid cycle scale, reduces CMV by 50%, and minimizes narrow pulse content compared to mainstream modulation strategies. These results confirm the theoretical predictions and underscore the practical advantages of DPS-SSVM in enhancing the performance and reliability of single-stage isolated converters in low-voltage applications.

## APPENDIX

The polynomial expressions of the two dependent variables in the modulation function are shown in (A1) and (A2), which are the result of series approximation, where the angles are both degrees

$$m_1(m,\phi_1) = \begin{pmatrix} -3.9\times10^{-2}+0.715m-2.65\times10^{-3}\phi_1+0.271m^2 \\ +3.85\times10^{-2}m\phi_1+5.85\times10^{-5}\phi_1^2-0.037m^2\phi_1 \\ -5.3\times10^{-4}m\phi_1^2-5.85\times10^{-7}\phi_1^3+3.4\times10^{-4}m^2\phi_1^2 \\ +1.24\times10^{-6}m\phi_1^3+4.45\times10^{-9}\phi_1^4 \end{pmatrix} \tag{A1}$$

$$\phi_{2\max}(\phi_1,m) = \begin{pmatrix} 12.18+0.98\phi_1-119m-0.05\phi_1^2-0.12\phi_1m \\ +224.5m^2+6.5\times10^{-4}\phi_1^3+0.07\phi_1^2m-4.6\phi_1m^2 \\ -1.23m^3-3.29\times10^{-6}\phi_1^4-1.66\times10^{-4}\phi_1^3m \\ -0.04\phi_1^2m^2+4.66\phi_1m^3-134.4m^4 \end{pmatrix} \tag{A2}$$

## REFERENCES


[1] N. D. Weise, G. Castelino, K. Basu, and N. Mohan, "A single-stage dual-active-bridge-based soft switched AC–DC converter with open-loop power factor correction and other advanced features," *IEEE Trans. Power Electron.*, vol. 29, no. 8, pp. 4007–4016, Aug. 2014.

[2] X. Li, F. Wu, G. Yang, and H. Liu, "Improved modulation strategy for single-phase isolated quasi-single-stage AC–DC converter to improve current characteristics," *IEEE Trans. Power Electron.*, vol. 35, no. 4, pp. 4296–4308, Apr. 2020.

[3] D. Sha, D. Zhang, and J. Zhang, "A single-stage dual-active-bridge AC–DC converter employing mode transition based on real-time calculation," *IEEE Trans. Power Electron.*, vol. 36, no. 9, pp. 10081–10088, Sep. 2021.

[4] J. Afsharian, D. Xu, B. Wu, B. Gong, and Z. Yang, "The optimal PWM modulation and commutation scheme for a three-phase isolated buck matrix-type rectifier," *IEEE Trans. Power Electron.*, vol. 33, no. 1, pp. 110–124, Jan. 2018.

[5] L. Schrittwieser, M. Leibl, and J. W. Kolar, "99% efficient isolated three-phase matrix-type DAB buck–boost PFC rectifier," *IEEE Trans. Power Electron.*, vol. 35, no. 1, pp. 138–157, Jan. 2020.

[6] D. Das, N. Weise, K. Basu, R. Baranwal, and N. Mohan, "A bidirectional soft-switched DAB-based single-stage three-phase AC–DC converter for V2G application," *IEEE Trans. Transp. Electrific.*, vol. 5, no. 1, pp. 186–199, Mar. 2019.

[7] F. Wu, K. Wang, G. Hu, Y. Shen, and S. Luo, "Overview of single-stage high-frequency isolated AC–DC converters and modulation strategies," *IEEE Trans. Power Electron.*, vol. 38, no. 2, pp. 1583–1598, Feb. 2023.

[8] X. Guo, Y. Yang, and X. Wang, "Optimal space vector modulation of current-source converter for DC-link current ripple reduction," *IEEE Trans. Ind. Electron.*, vol. 66, no. 3, pp. 1671–1680, Mar. 2019.

[9] J. Saha, R. K. Singh, and S. K. Panda, "Three-phase matrix-based isolated AC-DC converter for battery energy storage system," in *Proc. IEEE 12th Int. Symp. Power Electron. Distrib. Gener. Syst.*, Chicago, IL, USA, 2021, pp. 1–8.

[10] N. B. Y. Gorla, J. Saha, K. Jayraman, and S. K. Panda, "A modulation strategy with transformer leakage inductance energy management for a three-phase matrix-based isolated AC–DC converter," *IEEE J. Emerg. Sel. Topics Power Electron.*, vol. 11, no. 3, pp. 2780–2792, Jun. 2023.

[11] D. Varajão, R. Esteves Araújo, L. M. Miranda, and J. A. Peças Lopes, "Modulation strategy for a single-stage bidirectional and isolated AC–DC matrix converter for energy storage systems," *IEEE Trans. Ind. Electron.*, vol. 65, no. 4, pp. 3458–3468, Apr. 2018.

[12] M. A. Sayed, K. Suzuki, T. Takeshita, and W. Kitagawa, "PWM switching technique for three-phase bidirectional grid-tie DC–AC–AC converter with high-frequency isolation," *IEEE Trans. Power Electron.*, vol. 33, no. 1, pp. 845–858, Jan. 2018.

[13] F. Fang, H. Tian, and Y. Li, "SVM strategy for mitigating low-order harmonics in isolated AC–DC matrix converter," *IEEE Trans. Power Electron.*, vol. 36, no. 1, pp. 583–596, Jan. 2021.

[14] W. Hu, Y. Xie, Z. Wang, Z. Zhang, and Y. Guan, "A family of asymmetrical SVPWM schemes with normal and open-circuit fault-tolerant operation capability for a three-phase isolated AC–DC matrix converter," *IEEE Trans. Power Electron.*, vol. 37, no. 2, pp. 1788–1803, Feb. 2022.

[15] X. Li, F. Wu, G. Yang, H. Liu, and T. Meng, "Dual-period-decoupled space vector phase-shifted modulation for DAB-based three-phase single-stage AC–DC converter," *IEEE Trans. Power Electron.*, vol. 35, no. 6, pp. 6447–6457, Jun. 2020.

[16] F. Wu, X. Li, G. Wang, H. Liu, and Y. Dai, "Analysis of effect of grid harmonics and unbalance on DAB-based three-phase single-stage AC–DC converter and solutions," *IEEE J. Emerg. Sel. Topics Power Electron.*, vol. 10, no. 1, pp. 1192–1202, Feb. 2022.

[17] F. Wu, X. Li, G. Yang, H. Liu, and T. Meng, "Variable switching periods based space vector phase-shifted modulation for DAB based three-phase single-stage isolated AC–DC converter," *IEEE Trans. Power Electron.*, vol. 35, no. 12, pp. 13725–13734, Dec. 2020.

[18] X. Guo, L. Zhang, Y. Wei, and S. Wu, "A coordination control method for current stress reduction in high-frequency link matrix converter," *IEEE Trans. Ind. Electron.*, vol. 71, no. 9, pp. 9972–9981, Sep. 2024.

[19] F. Fang, H. Tian, and Y. Li, "Coordination control of modulation index and phase shift angle for current stress reduction in isolated AC–DC matrix converter," *IEEE Trans. Power Electron.*, vol. 36, no. 4, pp. 4585–4596, Apr. 2021.

[20] X. Li, F. Wu, G. Yang, H. Liu, and F. Meng, "Precise calculation method of vector dwell times for single-stage isolated three-phase buck-type rectifier to reduce grid current distortions," *IEEE J. Emerg. Sel. Topics Power Electron.*, vol. 8, no. 4, pp. 4457–4466, Dec. 2020.

[21] J. Song et al., "A modified space vector modulation for DC-side current ripple reduction in high-frequency link matrix converter," *IEEE Trans. Transp. Electrific.*, vol. 8, no. 4, pp. 4470–4481, Dec. 2022.

[22] W. Hu, Y. Xie, Y. Guan, Z. Wang, Z. Zhang, and J. Xu, "A novel volt-second self-balancing SVPWM scheme to eliminate steady-state DC bias for a three-phase isolated AC–DC matrix converter," *IEEE Trans. Power Electron.*, vol. 35, no. 11, pp. 11518–11532, Nov. 2020.

[23] D. Lan, P. Das, and S. K. Sahoo, "A high-frequency link matrix rectifier with a pure capacitive output filter in a discontinuous conduction mode," *IEEE Trans. Ind. Electron.*, vol. 67, no. 1, pp. 4–15, Jan. 2020.

[24] D. Lan, P. Das, C. Ye, S. K. Sahoo, and D. Srinivasan, "High-frequency link matrix rectifier in discontinuous conduction mode with reduced input current distortion," *IEEE Trans. Ind. Electron.*, vol. 68, no. 7, pp. 5517–5526, Jul. 2021.

[25] P. Jin, Y. Hu, G. Lei, Y. Guo, and J. Zhu, "A novel SVM strategy to reduce current stress of high-frequency link matrix converter," *IEEE Trans. Ind. Electron.*, vol. 71, no. 5, pp. 4652–4662, May 2024.

[26] Y. Hu, P. Jin, Y. Guo, G. Lei, and J. Zhu, "A new SVM strategy to suppress total harmonic distortion and current stress in HFLMCs," *IEEE Trans. Ind. Electron.*, vol. 71, no. 9, pp. 10512–10522, Sep. 2024.

[27] Y. Xu, Z. Wang, Y. Shen, Z. Zou, and F. Deng, "An improved modulation scheme of isolated matrix converter for common-mode voltage reduction and DC-bias current mitigation," *IEEE Trans. Ind. Electron.*, vol. 70, no. 12, pp. 12278–12287, Dec. 2023.

[28] H. Sun, T. Zhang, and J. Jiang, "Zero-vector-reconfiguration based SVPWM technique for ZVZCS and voltage spike suppression high-frequency link three-phase AC-DC converter," *IEEE Trans. Power Electron.*, vol. 39, no. 5, pp. 5536–5546, May 2024.

[29] D. Sal y Rosas, D. Chavez, and J. Tafur, "Quad-active-bridge resonant-type single-stage three-phase AC–DC converter: Modulation and control for V2G applications," *IEEE Trans. Power Electron.*, vol. 40, no. 7, pp. 9034–9047, Jul. 2025.